Physics in Medicine &
Biology

PAPER • OPEN ACCESS

2.5D imaging: obtaining depth information from 2D helium-beam radiographs*

To cite this article: Margareta Metzner *et al* 2025 *Phys. Med. Biol.* **70** 205017

IOP Publishing Phys. Med. Biol. 70 (2025) 205017 https://doi.org/10.1088/1361-6560/ae02de

Physics in Medicine & Biology

IPEM Institute of Physics and Engineering in Medicine

PAPER

2.5D imaging: obtaining depth information from 2D helium-beam radiographs*

OPEN ACCESS

RECEIVED
26 April 2025

REVISED
26 August 2025

ACCEPTED FOR PUBLICATION
3 September 2025

PUBLISHED
15 October 2025

Margareta Metzner[1,2,3,9,**], **Annika Schlechter**[1,2,3,9], **Daria Zhevachevska**[1,2,4], **Patrice Schlegel**[1,2,5,6], **Oliver Jäkel**[1,2,7,8], **Mária Martišíková**[1,2,10] **and Tim Gehrke**[1,2,10]

[1] Heidelberg Institute for Radiation Oncology (HIRO) and National Center for Research in Radiation Oncology (NCRO), Heidelberg, Germany
[2] German Cancer Research Center (DKFZ) Heidelberg, Division of Medical Physics in Radiation Oncology, Heidelberg, Germany
[3] Department of Physics and Astronomy, Heidelberg University, Heidelberg, Germany
[4] Medical Faculty Mannheim, Heidelberg University, Mannheim, Germany
[5] Heidelberg University, Institute of Computer Science, Heidelberg, Germany
[6] Medical faculty Heidelberg, Heidelberg University, Heidelberg, Germany
[7] Heidelberg Ion Beam Therapy Center (HIT), Department of Radiation Oncology, Heidelberg University Hospital, Heidelberg, Germany
[8] National Center for Tumor Diseases (NCT), NCT Heidelberg, a partnership between DKFZ and Heidelberg University Hospital, Heidelberg, Germany
[9] These authors share first authorship.
[10] These authors share last authorship.
[**] Author to whom any correspondence should be addressed.

E-mail: margareta.metzner@dkfz-heidelberg.de

Keywords: ion-beam imaging, Timepix detectors, proton therapy, particle therapy, particle radiography, helium ions, spatial resolution

Abstract

Objective. Ion-beam radiography has been proposed as a daily on-couch imaging modality for ion-beam radiotherapy range verification. However, an ion-beam radiograph only contains 2D information since it shows a projection of the patient along the beam direction. To extract depth information of anatomical changes from 2D helium-beam radiographs, we experimentally investigated the 2.5D imaging approach. *Approach.* At the Heidelberg ion-beam therapy center, we acquired helium-beam radiographs of a homogeneous plastic phantom and an anthropomorphic phantom. We changed the geometry of both phantoms to mimic anatomical changes and acquired data before and after the change. After reconstructing plane-of-interest difference images along depth in 1 mm steps, we analyzed the spatial resolution by means of the slanted edge approach and a method based on a median filter and Tenengrad focus measure. The depth of the maximum spatial resolution was then compared to the one where the change was introduced in the experiment and their difference was determined as measure of accuracy. *Main results.* For both the slanted edge and Tenengrad method, all accuracy values of the plastic phantom were below 11 mm. Furthermore, the found depth values of all but one gap position coincided with the ground truth position of the edge within the 2 σ uncertainty. In the anthropomorphic phantom, we reached a depth accuracy of 13^{+5}_{-7} mm. *Significance.* The 2.5D imaging approach, which was investigated experimentally for the first time in this work, offers a technique to estimate the depth of an anatomical change based on the acquisition of 2D ion-beam radiographs. This information is crucial to determine whether the change is located within the treatment field and thus impairs the treatment. 2.5D ion-beam radiography could therefore be used for daily on-couch imaging to monitor the anatomy of the patient and make ion-beam radiotherapy treatments more precise.

---

[*] Some methods presented in this publication are parts of: Schlechter, Annika, 2.5D Imaging: Accessing 3D information of a 2D ion-beam radiograph, Master's thesis, Heidelberg University, Germany, 2024.

1. Introduction

External ion-beam radiotherapy is a promising modality for precise cancer treatment (Levin *et al* 2005, Thariat *et al* 2013, Liang *et al* 2025). Since ions undergo fundamentally different interactions in the patient's tissue than the conventionally used photons, they also deposit their energy in a different way. Their dose-depth curve exhibits a sharp peak, the so-called Bragg peak, before the ions reach the end of their range and stop (Bragg and Kleeman 1905, Newhauser and Zhang 2015). Therefore, highly conformal dose distributions can be created with ion beams, the potential of which was already recognized in the 1940s by Wilson (1946). If these distributions are tailored to the patient anatomy, less physical dose is deposited in healthy tissue in comparison to conventional radiotherapy (Palm and Johansson 2007, Schulz-Ertner and Tsujii 2007, Schardt *et al* 2010, De Water *et al* 2011, Durante and Debus 2018). Thus, ion-beam radiotherapy treatments clearly hold the potential to lower the risk of side effects and secondary cancer for specific tumor sites (Paganetti *et al* 2012).

However, due to the steep gradients, conformal physical dose distributions are highly sensitive to uncertainties and their mitigation is of major importance (Knopf and Lomax 2013, Parodi and Polf 2018).

The main source for uncertainties is the potentially changing anatomy of the individual patient (Lomax 2020). In clinical practice, the spatial distribution of tissue types in the patient is determined by means of a planning x-ray computed tomography (CT) scan, which is acquired before the treatment starts. However, the patient anatomy can change during the treatment course of usually several weeks due to e.g. fillings of cavities, tumor shrinkage, or weight loss. This can then lead to an under-dosage of the tumor volume and/or over-dosage of healthy tissue and therefore a potentially worse treatment outcome.

Different technologies have been proposed to verify the range of the ion beams in the tissue of the patient regularly, among them ion-beam radiography (Knopf and Lomax 2013, Parodi and Polf 2018, Gianoli *et al* 2024). For this imaging modality, the beam is accelerated to a higher initial energy to traverse the patient and be detected on the opposite side with specialized detectors (Parodi 2014, Poludniowski *et al* 2015, Johnson 2017). The detected signal varies depending on the tissue traversed by the ions, enabling the reconstruction of a medical image in beams-eye view. This technology offers the advantage of on-couch imaging directly before the treatment starts and could therefore be used for adaptive ion-beam radiotherapy (Palaniappan *et al* 2021, 2022).

In clinical practice, ion-beam radiographs could replace the currently used x-ray based positioning images (Romero *et al* 1995, Schneider and Pedroni 1995, Hammi *et al* 2017) while depositing similar doses (Schneider and Pedroni 1995, Schulte *et al* 2005, Miller *et al* 2019, Collins-Fekete *et al* 2021). In addition to the application in patient positioning, the method could be used to detect and localize anatomical changes laterally, by comparing the ion-beam images between fractions. Since ion-beam radiographs are quantitative in terms of water-equivalent thickness (WET)[11], anatomical changes could also be quantified (Sarosiek 2021). This is especially important to assess the impact on the dose distribution.

However, the information about the depth of an anatomical change is not contained in a 2D radiograph due to the integration over the axis along the beam direction. For clinical application, it is important to know whether a change affects the treatment, that is if the change is located within the path of the treatment ions, or not. By means of a single ion-beam radiograph, changes in front of or behind the tumor cannot be distinguished, which might lead to a false positive triggering of a control CT and therefore additional dose to the patient.

To obtain depth information, several projections or alternatively an ion CT could be acquired, which would hold the disadvantage of additional dose to the patient, compared to a single ion-beam radiograph. Thus, the acquisition of an ion CT seems not reasonable at least on a daily basis.

Another technique to obtain depth information from ion-beam radiographs was recently proposed by Volz *et al* (2024). By analyzing simulated proton-beam radiographs of bone cubes in a water phantom, they investigated the so-called 'focus-stacking method' to improve the spatial resolution for objects with features at different depths. Determining the maximum spatial resolution of the bone cubes across all images reconstructed at various depths also allowed them to estimate the actual depth of the bone cubes, an approach that worked particularly well at the back of the phantom.

In this contribution, we are expanding the simulation-based investigations by initial experiments towards this concept. In contrast to Volz *et al* (2024), we use helium ions instead of protons. Furthermore, we advance the methodology for the depth determination by using improved filtering and analysis techniques.

The complete approach for depth determination from 2D ion-beam radiographs, which we call 2.5D imaging, could be used in clinical settings to obtain the depth of an anatomical change within the patient and

---

[11] corresponding to the integrated stopping power of the material divided by the one of water.

thereby allow the estimation of its impact on the dose distribution. Therefore, ion-beam radiography in combination with the 2.5D imaging approach could be used as a low-dose imaging modality to increase the precision of ion-beam radiotherapy treatments.

2. Material and methods

2.1. Detection system

The detection system (Amato *et al* 2020, Metzner *et al* 2024) shown in figure 1 utilizes Timepix detectors of the first generation (Llopart *et al* 2007) for both tracking and energy deposition measurements of single ions. The light-weight hybrid silicon pixel detectors consist of a 300 μm thin silicon layer, which is bump-bonded to a Timepix chip. The detectors were purchased from ADVACAM s.r.o. with an especially thinned down chip to reduce scattering within the detectors. The front (2) and back tracking unit (3) consist of two detectors each, all of them operated in time of arrival (ToA) mode. Using the center of mass coordinates of the single ion hits in the pixel matrix, their lateral position together with the ToA is obtained on these detectors. By searching for temporal coincidences with a maximum coincidence window of 400 ns, the position of single ions can be traced at four positions along the beam path. Using this information together with the cubic-spline-path reconstruction (Collins-Fekete *et al* 2015, 2017, Krah *et al* 2019), the most-likely path of each single ion within the imaged object can be approximated. This approach has been shown to improve spatial resolution in comparison to a straight line (Gehrke *et al* 2018b). In the energy deposition unit (5), one detector measures the time over threshold (ToT) of single ions. This quantity can be translated to energy deposition values (Jakubek 2011) and provides the image contrast. To obtain a time information also in that unit, the last detector measures ToA. The energy degrader (4), which is a 5.5 mm thick piece of copper, was included to improve the spatial resolution of the system and to operate as a safety buffer between the high energy deposition on the last detection unit and the object to be imaged (6) (Amato *et al* 2020).

In case images larger than the field of view of $14 \times 14\,\text{mm}^2$ are to be imaged, the object has to be mounted on a translation stage (7). Then, several sub-images are acquired in a tiled fashion and later combined during the post-processing (Metzner *et al* 2024).

2.2. Imaging experiments at the Heidelberg ion-beam therapy (HIT) center

At the Heidelberg ion-beam therapy center (HIT), ${}^{4}_{2}\text{He}^{2+}$ particles were used for all experiments. They were shown to provide a better spatial resolution than protons without disadvantages in terms of imaging dose under the constraint of an equal contrast to noise ratio (CNR) (Gehrke *et al* 2018a). Carbon ions were shown to offer even higher spatial resolution; however, they were connected to a higher imaging dose at equal CNR compared to protons or helium ions (Gehrke *et al* 2018a). The beam was set to a static pencil beam with a FWHM of 10.3 mm – 11.1 mm and an intensity of $10^4 - 10^5$ particles s^{-1}.

Since the detectors have a long dead time, the dose absorbed by the imaged object is rather high without any synchronization of the beam with the detectors. However, as newer detector generations (e.g. Timepix3) can be operated quasi dead-time free due to an improved readout, it is more meaningful to refer to the dose of the ions arriving in the active time, which we do throughout this work.

Helium-beam radiographs of two different phantoms were acquired: a geometric phantom and an anthropomorphic one. They are both depicted in figure 2 and will be separately described in the following.

The geometric phantom is shown in a photograph in figure 2(a) and schematically in figure 2(b). It consists of homogeneous slabs of polymethyl methacrylate (PMMA) with different thicknesses. One of these slabs was partly thinned down by 1.9 mm resulting in a sharp edge (marked with red solid arrow). The edge was positioned at a small angle of around 2° with respect to the detector matrix to enable an evaluation of the spatial resolution by means of the slanted edge method (Reichenbach *et al* 1991, Fujita *et al* 1992). In the following, we will refer to the thinned-down part as air gap. The total geometric thickness of the slabs is around 164 mm for the full phantom and 162 mm for the thinned down part. This corresponds roughly to WETs of 186 mm and 184 mm, which are e.g. relevant for tumor sites within a human head.

Two different regions of the phantom were imaged. Once, an image with the edge outside of the field of view (green rectangle in figures 2(a) and (b)) was acquired to obtain a reference image of the full homogeneous phantom. The blue region containing the edge was imaged five times. For each successive acquisition, the order of the slabs was varied resulting in a different depth of the edge within the otherwise homogeneous phantom (denoted with dashed red arrows in figure 2(b)). The middle of the 1.9 mm thick gap was positioned at depths of 1 mm, 40 mm, 83 m 123 mm, and 163 mm. Thus, including the reference we obtain images of six different configurations of the phantom. By comparing the images of the full phantom with the five other data sets, we can imitate the emptying of a cavity at five different depths of the phantom in a very simplified way. The images were acquired with a beam energy of 188.07 MeV u^{-1}.

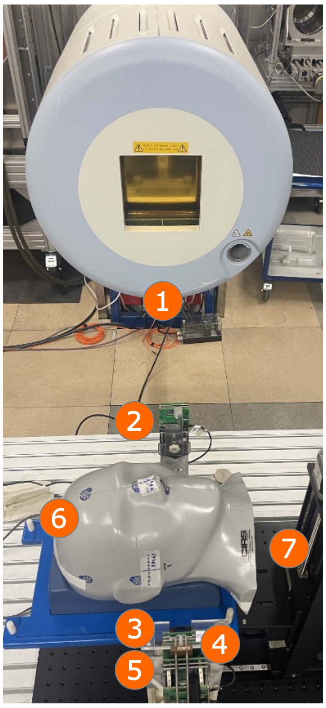

Figure 1. Experimental setup in front of the beam nozzle (1). The detection system consists of the front tracker (2), back tracker (3), energy degrader (4), and energy deposition unit (5) (Amato *et al* 2020). Between the two trackers, the imaged object (6) is mounted on a translation stage (7) .

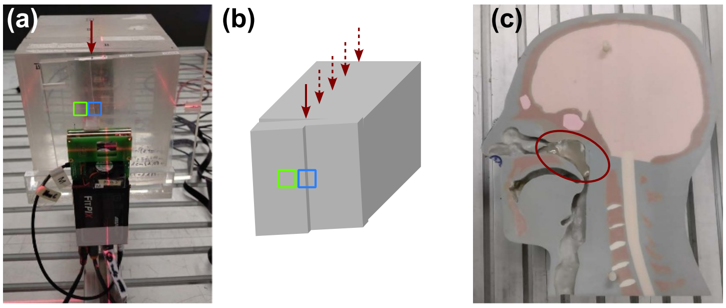

Figure 2. Phantoms imaged in this work. (a), (b) Photograph and schematic of the geometric phantom consisting of one slab with a step and several homogeneous slabs as built-up material. The edge marked by the red solid arrow divides the two steps which deviate by 1.9 mm in geometrical thickness. This step was positioned at an angle of approximately 2° with respect to the detector's pixel matrix and inserted at four additional depths (dashed red arrows in (b)) between the built-up material. Two different regions of this phantom were imaged: the green one containing only the homogeneous part and the blue region containing the edge successively at five different depths (i.e. six imaged configurations). (c) Anthropomorphic phantom, which was imaged twice: once in its normal configuration and once including a silicone insert in the nasopharynx (Schweins *et al* 2025) (red ellipse).

The anthropomorphic phantom CIRS 731-HN (Proton Therapy Dosimetry Head, Model 731-HN; CIRS, Norfolk, VA, USA) was used to investigate the method for a clinically realistic scenario. The phantom, which is shown in figure 2(c) can be taken apart in such a way, that one cavity is accessible. We introduced 6 g of silicone (marked in red) in the nasopharyngeal region to mimic an anatomical change (Schweins *et al* 2025). Also, for this phantom, we acquired a reference radiograph without the silicone.

Since the region to be imaged was heterogeneous and larger than the sensitive area of the Timepix detector, the data was acquired in a tiled manner using the energy painting algorithm and initial beam energies between 146.84 MeV u^{-1} and 178.13 MeV u^{-1}. The energies for each sub-region were selected based on the expected WET range in a projected x-ray CT scan of the phantom without the silicone insert (Metzner *et al* 2024, Metzner *et al* 2025). This prior information of estimated WETs will be available in form of a projected planning CT for the envisaged clinical applications as described in the introduction.

The analysis for the anthropomorphic phantom was conducted only with a subset of the measured data in order to achieve a clinically realistic dose.

2.3. Post-processing

The following is an outline of the data post-processing steps conducted: (1) translation of ToT values on detector 5 to energy deposition values (Jakubek 2011), (2) lateral alignment correction of the detectors, (3) merging of the information on all detectors connected to the same ion, and (4) calculation of the most-likely path of each single ion employing the cubic-spline path algorithm (Collins-Fekete *et al* 2015, 2017, Krah *et al* 2019). Subsequently, plane-of-interest binned (PIB) images (Schneider and Pedroni 1994, Rit *et al* 2013, Gehrke *et al* 2018a, Volz *et al* 2020) were reconstructed in 1 mm-spaced depths by evaluating the cubic spline paths in these depths and binning the particles accordingly into pixels. Furthermore, an along-path reconstructed (APR) image (Gehrke *et al* 2018a) was obtained, which contains information from all depths and provides better CNR (Gehrke *et al* 2018a, Volz *et al* 2020), as similarly found for the maximum-likelihood radiography (Collins-Fekete *et al* 2016). Both PIB and APR images were then subjected to a dE-WET calibration (Knobloch *et al* 2022). Finally, the energy painting algorithm (Metzner *et al* 2024) was applied for the anthropomorphic phantom to image a WET interval of around 70 mm with high precision. Along this whole post-processing chain, several filtering steps were performed. For details, please refer to Metzner *et al* (2024).

To insert the piece of silicone inside of the anthropomorphic phantom, the latter had to be taken apart and re-positioned. Since perfect re-positioning could not be achieved using the available in-room laser positioning system, a 2D image registration algorithm based on mutual information (Mattes *et al* 2001), available as part of the DKFZ developed MatchPoint (Floca 2009) framework, was used to register the APR image with the silicone insert to the reference APR image without the insert. The resulting transformation matrix was then applied to all PIB images of the data set with the silicone insert.

2.4. 2.5D imaging: depth detection of anatomical changes

A well-known and frequently cited disadvantage of ions for imaging is multiple coulomb scattering, which impairs the spatial resolution of each ion image (Knopf and Lomax 2013, Volz *et al* 2020). Ions experience many scattering events and get deflected e.g. within a phantom.

In the example shown in figure 3(a), a schematic ion beam traverses a phantom, which consists of homogeneous material and two features at a certain depth which are assumed to have different densities from each other and their surrounding.

Because of many scattering events, each ion carries the accumulated information from multiple lateral positions of the traversed object. The measured WET information, detected as energy deposition at one single detector location, contains contributions of other lateral locations, which leads to blurring. To correct for this well-known effect in a subsequent analysis, trackers can be employed. The most likely path (figure 3(a)) calculated based on the measured positions in the trackers can be evaluated in each depth of the phantom (figure 3(b)). Then, the energy deposition value, which is measured on the last detector unit in the experiment and encoded in the color of the ions' paths, is assigned to the pixel where the ion was approximately located laterally according to the cubic spline path at that depth (figure 3(c)). This reconstruction was previously referred to as plane-of-interest binning (PIB) (Schneider and Pedroni 1994, Rit *et al* 2013, Gehrke *et al* 2018a, Volz *et al* 2020).

In contrast to slices of an ion CT, PIB images as well as APR images show values integrated along the beam direction. The impact of these reconstruction methods is limited to the spatial binning of the ions and does not affect the single-ion energy deposition or, after calibration, the WET values themselves.

In the example shown in figure 3, the differently colored ions are assigned to separate regions in the image reconstructed the middle of the phantom which enables a sharp transition. If the image is reconstructed further away from the actual depth of the features, the ions, which carry different WET information, start to mix due to their bent paths. Hence, the edge between the two different WET values is blurred in these depths. This example motivates the hypothesis that the spatial resolution can be assumed to be highest in an PIB image, which was reconstructed at a depth close to the actual depth of the feature (figure 3(d)). This hypothesis has already been validated by several studies (Rit *et al* 2013, Volz *et al* 2020, Khellaf *et al* 2022). Volz *et al* (2024) proposed to find the maximum spatial resolution over all PIB images reconstructed in different depths to thereby access the depth of a feature (figure 3(e)).

In contrast to the named work, our objective is to determine the depth at which a change occured within a phantom, rather than the depth of a volumetric feature itself. This is of particular relevance for clinical applications. Therefore, we also acquired a reference data set without an anatomical change. All data sets, including the reference, are separately reconstructed as PIB images with a spacing of 1 mm over the whole phantom. Before we investigate the spatial resolution of the images showing the air gap, we first subtract the corresponding reference image in each depth. In this way, we obtain images reconstructed at different depths showing only the anatomical change.

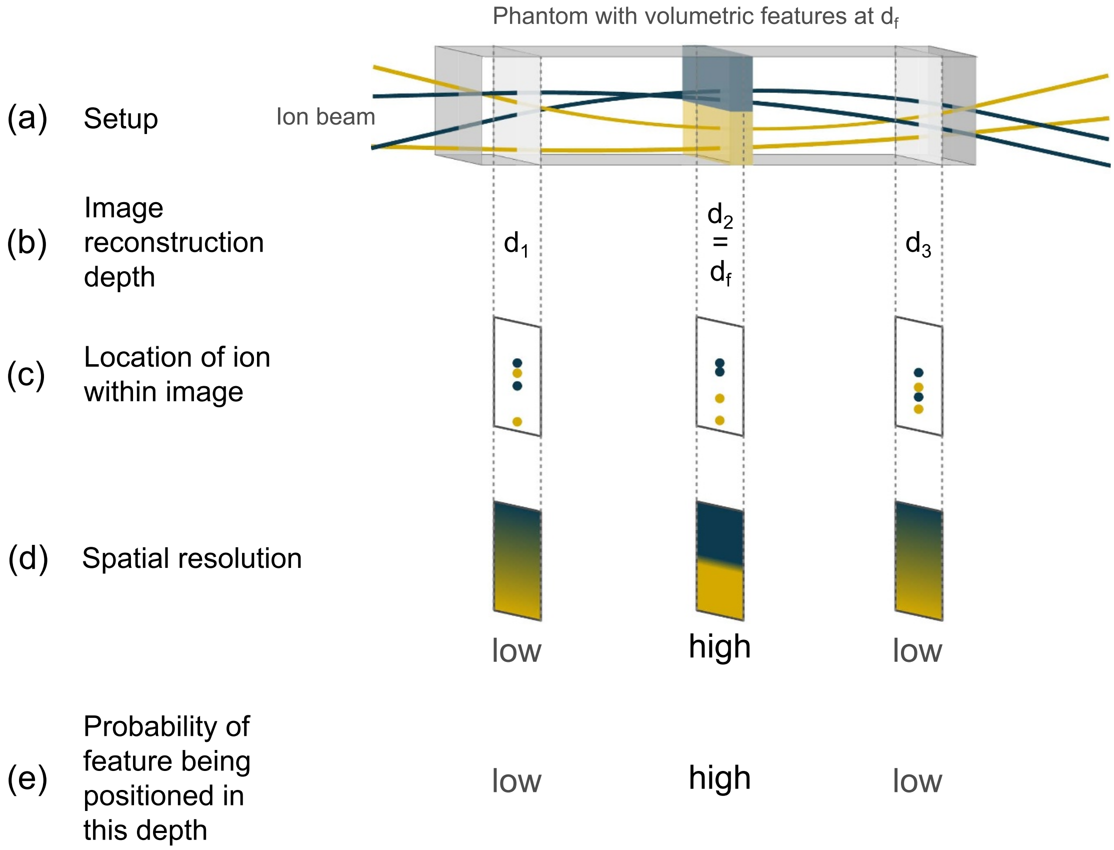

Figure 3. Schematic showing the idea behind 2.5D imaging. (a) Four ions travel through the phantom which contains volumetric features with different densities than their surroundings, shown here as blue and yellow boxes. Due to the density differences, one half of the ions traverses a different WET than the other, which is why their path is marked with the respective color. (b) Images in different depths can be reconstructed (Schneider and Pedroni 1994, Rit *et al* 2013, Gehrke *et al* 2018a, Volz *et al* 2020). (c) For this purpose, the lateral location of each single ion in the respective depth is determined and its WET value mapped to it. (d) Among the three images, the one reconstructed at the depth of the volumetric features has the highest spatial resolution, since at this location the ions are assigned to the lateral position of the box which they traversed. (Rit *et al* 2013, Volz *et al* 2020, Khellaf *et al* 2022). (e) The spatial resolution can thus be used as a metric to determine the depth of the feature (Volz *et al* 2024).

In case of the geometric phantom, we firstly assessed the angle between the slanted edge and the detector matrix in the difference APR image. For this purpose, we performed error function fits on sets of three-pixel rows to find the center of the edge in each group of rows. These centers were then used as input for a linear fit that determined the edge's coordinates. We set the found angles as fixed parameter for the slanted edge analysis with the PIB images to reduce the impact of their noise on the analysis, especially for the low spatial resolution values.

Lastly, we determined the spatial resolution of the PIB images using the slanted edge method (Reichenbach *et al* 1991, Fujita *et al* 1992), which is a well-established technique for this purpose. We used a pixel size of 0.22 mm × 0.22 mm in order to provide enough pixel rows for the oversampling of the edge spread function (ESF). Based on that oversampled ESF, we determined the modulation transfer function (MTF) at 10% contrast to obtain the spatial resolution. This method is particularly powerful, since it provides a quantitative measure of spatial resolution that enables to assess the system's performance and to compare it with other systems or imaging modalities. However, it can only be used for the very specific case of a slanted edge, which does not occur in clinical scenarios. Since it is not applicable to anthropomorphic changes, we additionally investigated a methodology based on various image processing operators. In contrast to the approach of Volz *et al* (2024) several changes were made, which are pointed out in the appendix. For an assessment of the different methodologies, please refer to that chapter.

The PIB images of both the geometric phantom (discretized with a pixel size of 0.44 mm × 0.44 mm) and the anthropomorphic phantom (1 mm × 1 mm) were analyzed with this second approach. First, the three outermost pixel rows were excluded, as they can be deteriorated by edge effects and, in the case of the anthropomorphic phantom, by inaccuracies introduced during image registration. We chose to use a median filter (Tukey *et al* 1977) to reduce image noise due to its robustness to impulse noise and edge preservation properties. The filter kernel size was chosen at a value corresponding to 3 mm × 3 mm, which represents a compromise between noise reduction and edge preservation.

In an effort to identify the PIB image in the series along the depth axis that exhibits the sharpest gradients across the entire image (i.e. the highest spatial resolution), we evaluated each image based on its Tenengrad (Tenenbaum 1971, Schlag *et al* 1983) score. The Tenengrad metric accumulates the strength of image gradients into a single quantitative measure of sharpness. It uses the Sobel operator $\hat{S}_x$ and $\hat{S}_y$ (Danielsson 1990)

$$\hat{S}_x = \begin{pmatrix} 1 \\ 2 \\ 1 \end{pmatrix} \begin{pmatrix} -1 & 0 & 1 \end{pmatrix}, \qquad \hat{S}_y = \begin{pmatrix} -1 \\ 0 \\ 1 \end{pmatrix} \begin{pmatrix} 1 & 2 & 1 \end{pmatrix} \tag{1}$$

to compute horizontal and vertical gradients G_x and G_y by convolving both Sobel operators with the image I

$$G_x(x,y) = \hat{S}_x * I(x,y), \quad G_y(x,y) = \hat{S}_y * I(x,y) . \tag{2}$$

The results are then combined to obtain the gradient magnitude M at each pixel

$$M(x,y) = G_x(x,y)^2 + G_y(x,y)^2 , \tag{3}$$

where the squares are calculated matrix-element wise. Our final Tenengrad score is computed by calculating the average gradient magnitude over the entire image

$$\text{TENG} = \langle M(x,y) \rangle . \tag{4}$$

The final score reflects the overall presence and intensity of edges, with higher values indicating greater edge clarity.

For both methodologies, a Savitzky–Golay filter (Savitzky and Golay 1964) of second order was used to smooth the spatial resolution or Tenengrad score, respectively, over depth. Following Volz *et al* (2024), we used a window size of 11 mm. The 2 σ interval divided by the square root of the window size serves as our estimate for the uncertainty. The depth with the highest value in the smoothed curve then corresponds to the estimated depth where the anatomical change probably occurred.

3. Results

In this work, we experimentally investigated the potential of the 2.5D imaging approach to estimate the depth of an anatomical change occurring during the course of an ion-beam radiotherapy treatment. Firstly, we assessed the method in a homogeneous phantom for which we physically simulated an anatomical change by consecutively inserting an air gap at different depths. Then, we advanced the validation of our 2.5D imaging approach to a more clinically realistic case of an anthropomorphic phantom. Here, we placed a silicone insert in the nasopharyngeal cavity.

The geometric PMMA phantom was imaged in six different configurations: one producing a reference measurement of the homogenous phantom with no cavities, and five others with the edge of the air gap positioned at different depths along the beam axis.

The resulting difference images of three exemplary air gap positions with respect to the reference image are shown in figure 4(a) for different reconstruction depths. The pixel size is set to 0.44 mm × 0.44 mm as a compromise between noise and pixelation for the images with doses between (0.8 ± 0.6) mGy and (1.2 ± 0.8) mGy. In all images, the difference in WET of (2.24 ± 0.10) mm caused by the air gap is clearly visible and reflected in the absolute values of the difference image.

In figure 4(b), the oversampled ESFs (OESF) of the different reconstruction depths are shown together for each experimental depth of the air gap. The OESFs are plotted against their distance from the middle of the edge in each experiment in order to facilitate their comparability.

In figure 4(c), the corresponding MTFs are depicted. If the MTF at 10% is determined, the spatial resolution can be obtained quantitatively for all three reconstruction depths shown in this figure. In figure 4, it can be seen that the highest spatial resolution is achieved on the diagonal, where the reconstruction depth coincides with the depth where the gap was actually located at.

If reconstruction depths with 1 mm spacing spanning from the front of the phantom to its back are considered, the spatial resolution can be plotted against the reconstruction depth. The result is shown in figure 5. The five data sets with different gap positions are all plotted in a different color and the actual position of the air gap is marked with the vertical bar in the background. The spatial resolution for each reconstructed depth is shown as a small dot, the smoothed curve as a solid line and the corresponding 2 σ uncertainty as the envelope. The depth of the maximum of the curve is marked with a triangle.

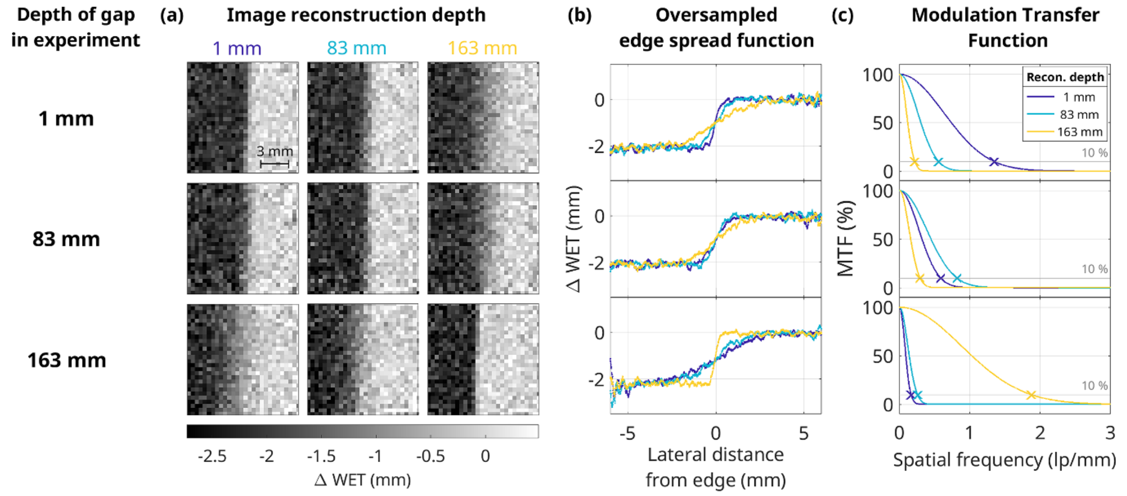

Figure 4. 2.5D images of a slanted edge and image characteristics. All data is shown for a 1.9 mm thick air gap within a homogeneous phantom, where the middle of the gap was positioned at 1 mm, 83 mm and 163 mm depth, respectively. (a) For each of the different experimental gap positions (rows) the difference images with respect to the reference are reconstructed in different depths (columns). (b) The oversampled edge spread function (OESF) is shown for all reconstruction depths. (c) The modulation transfer function (MTF) at 10% contrast is determined to assess the spatial resolution in absolute terms.

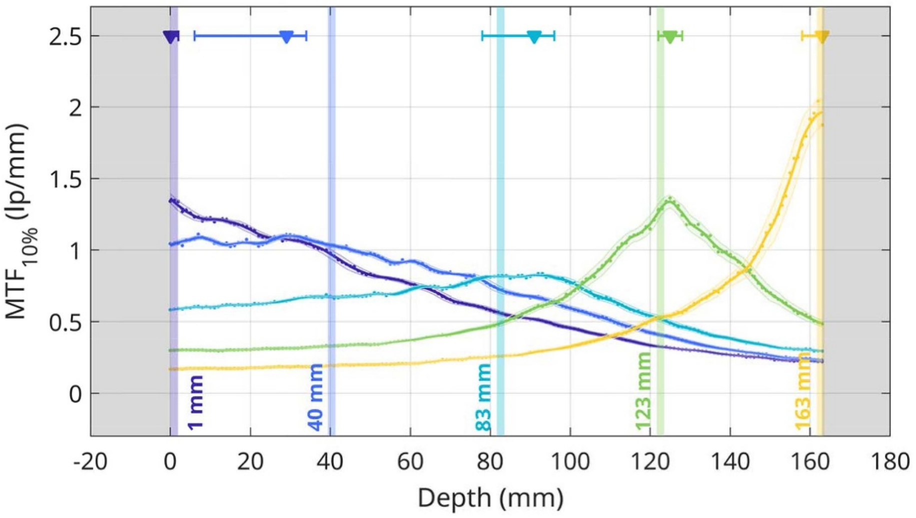

Figure 5. 2.5D depth detection of a 1.9 mm air gap within a homogeneous phantom using the slanted edge method. The experiment was conducted five times (one color denoting one experiment), where the middle of the 1.9 mm gap was positioned at 1 mm, 40 mm, 83 mm, 123 mm and 163 mm, respectively (vertical bars). The spatial resolution of the difference image determined with the slanted edge method (Reichenbach *et al* 1991, Fujita *et al* 1992) is marked with small dots. The smoothed curve together with its 2 σ uncertainty is shown as a continuous line and envelope, respectively. The found depth of the maximum spatial resolution is marked with a triangle together with its uncertainties.

The maximum spatial resolution for all five gap positions is listed in table 1 together with the corresponding reconstruction depth. It is similar to the depth where the gap was actually located at for all five data sets. If the different gap positions are compared, it becomes apparent that overall, the spatial resolution in absolute terms is the lowest for the gap in the middle of the phantom, whereas it is highest in the back of the phantom for our particular experimental setup.

The slanted edge method can only be used for very specific images showing a slanted edge (Reichenbach *et al* 1991, Fujita *et al* 1992). Thus, we additionally performed the 2.5D depth analysis on the same data set with another method, which we call Tenengrad method. As this method is capable of producing a score for any image, it is not limited by the type of imaged object.

Analogously to figure 5, in figure 6 the Tenengrad score, which is a measure for the gradients present in the image, is plotted against the reconstruction depth of the images. Overall, figure 6 closely resembles figure 5. Only the distribution of data points is slightly noisier for the Tenengrad method. To compare the accuracy of the two methods quantitatively, the difference between the depth of the maximum spatial

Table 1. Maximum spatial resolution (SR) and corresponding reconstruction depth (RD) of the slanted edge for all five experimental depths. The edge is caused by a 1.9 mm air gap within a 163 mm thick PMMA phantom and was imaged consecutively five times with the gap being positioned in different depths.

Depth of gap in experiment (mm)	Maximum SR (lp/mm)	Corresponding RD (mm)
0.0 – 1.9	1.36 ± 0.04	0^{+2}_{-0}
39.4 – 42.3	1.099 ± 0.010	29^{+5}_{-23}
81.7 – 83.6	0.823 ± 0.007	91^{+5}_{-13}
121.7 – 123.6	1.34 ± 0.05	125^{+3}_{-3}
161.7 – 163.6	1.97 ± 0.09	163^{+0}_{-5}

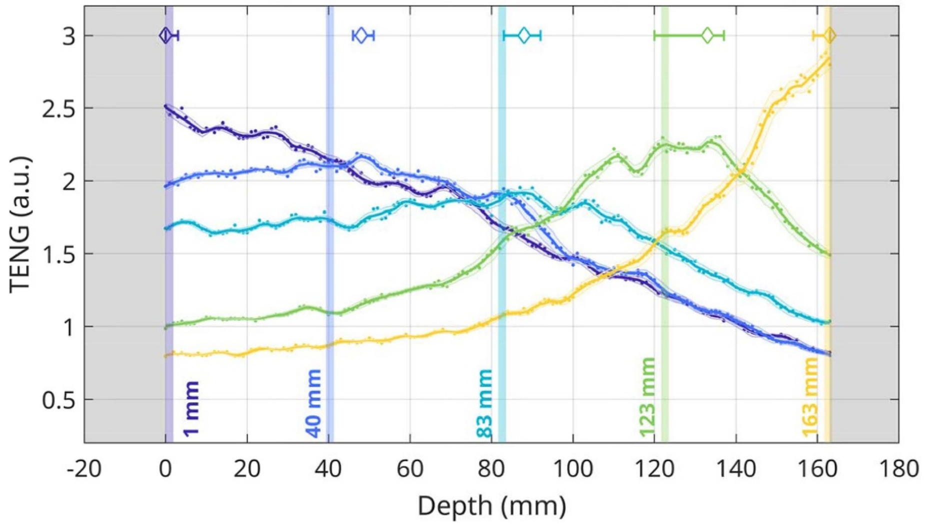

Figure 6. 2.5D depth detection of a 1.9 mm air gap within a homogeneous phantom using the Tenengrad method. The experiment was conducted five times (one color denoting one experiment), where the middle of the 1.9 mm gap was positioned at 1 mm, 40 mm, 83 mm, 123 mm and 163 mm, respectively (vertical bars). The Tenengrad score (Tenenbaum 1971, Schlag *et al* 1983) of the difference images with respect to the full phantom is marked with small dots over depth. The smoothed curve together with its 2 σ uncertainty is shown as a continuous line and envelope, respectively. The found depth of the maximum of the Tenengrad score is marked with a diamond together with its uncertainties.

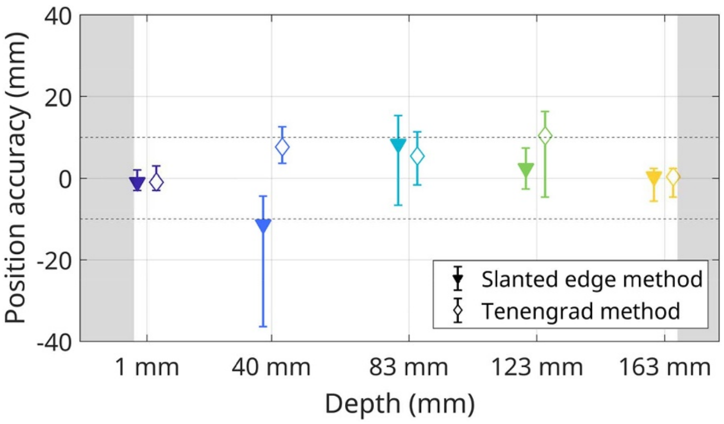

Figure 7. Accuracy of 2.5D depth detection. The difference between the depth of the maximum spatial resolution or Tenengrad score, respectively, and the actual depth of the gap in the experiment is shown for the slanted edge and Tenengrad method for all five gap positions.

resolution or Tenengrad score, respectively, and the actual position of the air gap was calculated for all five data sets (with different positions of the air gap) and for both methods. The resulting accuracy values are shown in figure 7. Two horizontal lines drawn at −10 mm and 10 mm mark the envisaged accuracy limits for clinical application.

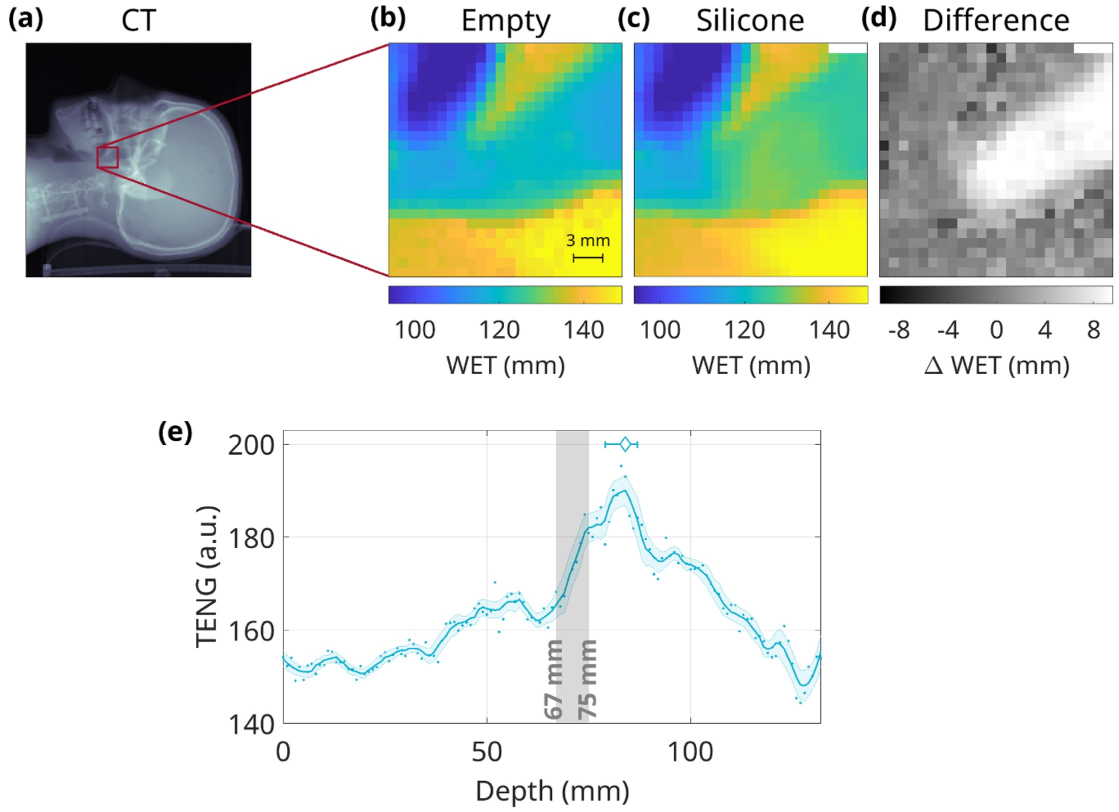

Figure 8. 2.5D depth detection of a cavity filling within an anthropomorphic phantom using the Tenengrad method. (a) Projected CT scan with imaged region marked by red rectangle. (b) Along-path reconstructed helium-beam radiograph of the marked region. (c) Along-path reconstructed helium-beam radiograph of the marked region with a silicone insert in nasopharyngeal cavity. (d) Difference image between both helium-beam radiographs. (e) Tenengrad score of the difference images plotted over depth. The smoothed curve together with the 2 σ uncertainty is shown as a continuous line and envelope, respectively. The depth of the maximum Tenengrad score is marked with a diamond together with its uncertainties. The silicone insert spanned from 67 to 75 mm depth within the phantom.

To assess the 2.5D imaging approach for a more complex case, an anthropomorphic head phantom was used. In figure 8(a), the imaged region is marked in a projected CT scan of the CIRS 731-HN phantom in its normal configuration. The helium-beam radiograph of that region is shown in figure 8(b), which is referred to as reference image in the following. The along-path reconstruction (APR) was used to obtain this low-noise image with a pixel size of 1 mm × 1 mm and a dose of (270 ± 170) μGy. In figure 8(c), a helium-beam radiograph of the same region of the phantom with a different configuration is shown. In this experiment, we inserted a piece of silicone into the nasopharyngeal cavity, which is accessible if the phantom is taken apart. The APR image of the filled cavity, which was acquired with the same parameters and dose, was registered to the reference image in order to mitigate differences due to minor deviations in the positioning.

Visually, higher WET values due to the addition of the silicone insert can be distinguished in the middle of the picture which turned yellow/green in c and was previously blue in b. To extract the WET of the silicone insert, the difference image was calculated (figure 8(d)). Here, the silicone insert clearly exceeds the noise in the rest of the picture. The silicone contributed with a maximum WET of around 8 mm.

Analogous to the previous analysis, we applied the Tenengrad method to the PIB difference images in order to determine the maximum Tenengrad score over 1 mm-spaced reconstruction depths. The corresponding data is shown in figure 8(e) in the same ways as in figures 5 and 6.

The maximum of the Tenengrad score is found to lie at 84^{+3}_{-5} mm. Since the middle of the 8 mm thick silicone insert was positioned at a depth of (71 ± 2) mm, the estimated depth has an accuracy of 13^{+5}_{-7} mm.

4. Discussion

In the work presented here, we experimentally investigated the 2.5D imaging approach to assess the depth of a change within a phantom from various reconstructions of 2D helium-beam radiographs.

The concept of analyzing a sequence of proton radiographs for spatial resolution improvements and depth detection was recently investigated by Volz *et al* (2024) in a Monte Carlo study. We conducted measurements to assess the capability and accuracy of this method experimentally, for which we used helium ions. We refined the methodology in several aspects. Instead of using a Gaussian filter, we smoothed our images by means of a median filter. Furthermore, instead of a Laplacian kernel we employ the Tenengrad score (Tenenbaum 1971, Schlag *et al* 1983), an object-agnostic image sharpness metric based on the accumulation of image gradients extracted by the Sobel operator (see equations (1)–(4)). Both changes reduced the method's sensitivity to noise (see appendix). Additionally, we presented the first validation of the metric-based approach against the well-established slanted edge method.

In figures 4–6, it can be seen that the maximum spatial resolution or Tenengrad score is reached close to the depth where the gap was actually located at. This experimentally confirms the results, which were previously found by means of Monte Carlo simulations (Rit *et al* 2013, Volz *et al* 2020, 2024, Khellaf *et al* 2022).

It is worth noting that in our work the depth detection with 2D ion radiographs was investigated the first time with helium ions. The authors chose this ion type because 2.5D imaging is thought of as an extension of ion-beam radiography and helium ions offer overall better image quality in terms of spatial resolution (Volz *et al* 2017, Gehrke *et al* 2018a). It is remarkable, that the 2.5D imaging technique also worked with helium ions. They scatter less than protons, which is however essential for the method. On the other hand, it is hypothesized that the minimum-to-maximum ratio of the spatial resolution over depth might be similar for helium ions and protons, although the spatial resolution of helium ions is generally shifted towards higher values.

The curves in figures 5 and 6 resulting from the slanted edge and Tenengrad methods, respectively, as well as their related accuracy values in figure 7 show a high degree of agreement. We therefore conclude, that applying the Tenengrad metric is a valid way to determine the spatial resolution for the 2.5D imaging approach, since it yields similar results to the well-established method of $\mathrm{MTF}_{10\%}$ determination using a slanted edge. Due to its applicability to any imaged object, it is therefore proposed as the suited metric for clinical use.

Since the purpose of the 2.5D method would be to deduce whether a change happened within the path of the treatment ions, the authors consider an accuracy and precision of around 1 cm to be sufficient. In figures 5 and 6, it can be seen that the accuracy and precision of our experimentally acquired values are satisfactory for the purpose of depth detection in ion-beam radiotherapy treatments. All accuracy values were determined to lie below 11 mm. All ground truth depths are within the $2\,\sigma$ uncertainty intervals of the estimated positions. Only the value for the gap at 40 mm determined with both methods does not coincide with the ground truth value within the uncertainty. This is in agreement with the findings of Volz *et al* (2024) who also found the least accurate depth determination for their edge at 50 mm depth.

In the simulation studies of Volz *et al* (2020), Khellaf *et al* (2022), it can be seen that the spatial resolution of a shallowly positioned edge is similar at the front surface and its actual depth causing noise to have a high impact on depth detection in this region. Our accuracy of around 10 mm for the gap at 40 mm quantitatively agrees with the one published in Volz *et al* (2020), where the highest spatial resolution of a feature in the first half of the phantom was found to occur up to 10 mm before its actual position. The lower accuracy at this depth seems therefore to be rather caused by a more fundamental characteristic of the ion paths than by our detection system.

In contrast to previous studies (Gehrke *et al* 2018a, Khellaf *et al* 2022), a higher spatial resolution was achieved in the back of the phantom compared to the front. In these previous works, the spatial resolution in the very front of the phantom was found to be the highest due to less multiple coulomb scattering at higher energies.

In our setup, due to technical reasons the front tracker was around two times further away than the rear tracker, having a distance to the phantom of 60 mm instead of to 34 mm. Larger position uncertainties caused by less accurate projections at the front surface of the phantom (Bopp *et al* 2014) led to overall flatter curves at shallow depths compared to the results shown in Khellaf *et al* (2022) where the trackers were positioned symmetrically.

Compared to Gehrke *et al* (2018a), we used higher initial beam energies and an energy degrader (Amato *et al* 2020). The overall higher velocities of the ions especially improved the spatial resolution in the back of the phantom. With the setup in Gehrke *et al* (2018a), the ions were close to the end of their range on the rear tracker, which led to more scattering and therefore higher uncertainties connected to the path estimates at greater depths.

If we compare our absolute values regarding the spatial resolution, we reach very similar values compared to Volz *et al* (2024). The effect of the use of a real detector setup instead of perfect tracking detectors right at the surface of the phantom, but on the other hand helium ions instead of protons (at least 55% better spatial resolution due to less scattering (Volz *et al* 2017, Gehrke *et al* 2018a)) seem to have approximately cancelled out.

Also Khellaf *et al* (2022) published spatial resolution values for images generated with a simulated proton beam. They simulated a realistic detector, however with a more than four times larger pixel pitch than ours. Additionally, they placed their detectors around four times further away from the phantom, which indeed is a more realistic distance for clinical use. Primarily due to the named three reasons, we reached significantly better spatial resolution values.

Having reached satisfactory results with the homogeneous PMMA phantom, we also applied the 2.5D imaging approach to an anthropomorphic head phantom. In the difference image, the silicone insert is clearly visible and its WET can be quantitatively assessed. This is a major advantage of ion imaging techniques compared to other range monitoring approaches, for the latter of which a change in the signal cannot easily be connected to a quantification of the anatomical change. In clinics, the WET of the change could help to classify whether it is significant with respect to the safety margins and if further action is indicated.

Since the images of the anthropomorphic phantom were acquired with a rather low dose of around (270 ± 170) μGy, the difference image in figure 8(d) shows some noise. Additionally, some small structures outside of the region, where the silicone was located, could be caused by rotations of the phantom around the two axes orthogonal to the beam, which could not be corrected for by the 2D image registration. Due to a slight rotation (1.5°) and translation (0.01 mm and -0.20 mm) in the image plane, three pixels in the upper right corner are empty in the registered image containing the silicone insert and, consequently, in the difference image.

In the plot showing the Tenengrad score against depth (see figure 8(e)), a maximum is clearly visible. The accuracy of the depth detection of 13^{+5}_{-7} mm is still satisfying considering the complex anatomy at the imaged region where the WET varied by around 70 mm within a field of view of 24 mm × 24 mm. Also here, we reach an accuracy which is useful for clinical application while employing a reasonable pixel size of 1 mm × 1 mm and a dose of (270 ± 170) μGy.

Due to the accessibility of the nasopharyngeal cavity in the middle of the phantom, there fortunately was an option to emulate an anatomical change within the anthropomorphic head phantom available at HIT. Since the authors evaluated this cavity to be a relevant region e.g. for treatments of skull base tumors, we decided to image it along the direction of a field entering the patient orthogonally from the left. In this way, we obtained a scenario which can realistically occur in clinics.

For skull base treatments, fillings of the cavity and fast responding or growing tumors pose a major challenge. The amount of cavity filling in our experiment was chosen rather generous (6 g). The WET of changes due to swelling or mucus caused by a cold is likely to be smaller. However, the WET difference observed for fast responding tumors, can be comparable (Barker Jr *et al* 2004).

Theoretically, the 2.5D imaging method can be applied to any body site which is suited for ion imaging in general. The practical limitations of the 2.5D method, e.g. with respect to the heterogeneity of the body sites or the movement of a target could be investigated by means of simulations.

In our presented analysis, only one anatomical change was introduced. In clinical reality, many changes of different extent can be present. If changes occur laterally separated from each other, a mask based on the WET difference could be used to evaluate the Tenengrad separately for each region containing a change. If changes overlap laterally and cannot be distinguished along depth, additional information e.g. the orientation of the gradients could be incorporated into the analysis. Also, the robustness of the method against remaining mispositioning despite the image registration should be investigated. Another promising direction involves studying the detectability of feature displacements along depth due to anatomical changes. Adjusting and testing the methodology for the mentioned aspects will be subject of future investigations.

Naturally, the 2.5D imaging approach is also applicable to other ion imaging systems employing trackers. Some parameters e.g. concerning the image filters might need some adjustments due to other image characteristics in terms of spatial resolution and CNR. Since carbon ions are also of interest for the ion-beam imaging community (Rinaldi *et al* 2014, Gianoli *et al* 2020, Kopp *et al* 2020, Simard *et al* 2025), future investigations could extend to that ion type. It might be worthwhile to find the type of ion for which the 2.5D imaging technique starts to fail due to the negligible scattering.

Some practical caveats remain for the presented detection system. The long dead time of the detectors will be solved by the use of Timepix 3 detectors, which we are planning to use in the near future. Furthermore, the movement of the phantom between the detection units is not practicable for clinical use. Therefore, a movement of the detection system together with the beam would be a solution worth testing. In that way, we could mimic larger effective areas while circumventing the cost intensive purchasing of larger arrays of Timepix detectors. If these challenges of only technical nature are addressed, we think the detection system, which offers an excellent spatial and WET resolution, might be a promising prototype for clinical imaging.

5. Conclusion

This study experimentally investigated the concept of 2.5D imaging. By determining the maximum spatial resolution over the reconstruction depth of 2D helium-beam radiographs, the actual depth of a change within head-sized phantoms could be determined with an accuracy of below 13 mm. The concept previously introduced by Volz *et al* (2024) by means of Monte Carlo simulations with a proton beam could be reproduced experimentally for the first time with helium ions in simple geometric phantoms as well as in an anthropomorphic head phantom. Furthermore, we were able to reduce the method's sensitivity to noise by employing a different filter strategy. We introduced a metric from the machine vision domain, the Tenengrad metric, for object-agnostic sharpness assessment in images, which we successfully applied and evaluated for depth detection.

The authors consider the 2.5D imaging approach a promising tool for daily on-couch imaging of the patient. The images allow to be compared between treatment fractions and thereby anatomical changes as well as patient positioning errors could be detected. With the depth information from the 2.5D imaging approach, the relevance of the anatomical change for the treatment could be classified without any drawbacks in terms of dose to the patient. Therefore, the 2.5D imaging approach proceeds as a low-dose imaging technique to make ion-beam radiotherapy more precise.

Data availability statement

The data cannot be made publicly available upon publication because they are not available in a format that is sufficiently accessible or reusable by other researchers. The data that support the findings of this study are available upon reasonable request from the authors.

Acknowledgments

The authors would like to thank Benjamin Ackermann for helping us with the handling of the CIRS phantom and Rebekka Kirchgässner, Maike Saphörster, Alexander Wiegand and Ferisya Sari for helping us with the experiments. We would also like to thank Stephan Brons and the accelerator team at HIT for the special beam settings and the support regarding our experiments. Furthermore, we would like to acknowledge Giulia Arico and Lennart Volz for measuring the WET of the PMMA slabs. Also, we would like to thank Lennart Volz for the discussions about the 2.5D imaging project. Ralf Floca, Stephen Schaumann and Erik Bartelme are thanked for their support regarding the image registrations. Margareta Metzner was funded by the DKFZ International PhD Program. Patrice Schlegel was funded by HIDSS4Health. Tim Gehrke was partially funded by the Deutsche Forschungsgemeinschaft (DFG, German Research Foundation)-Project No.: 426970603 and by the Federal Ministry of Research, Technology and Space within the program 'Bildgeführte Diagnostik und Therapie–Neue Wege in der Intervention' under Grant 13GW0436A (ARTEMIS).

Conflict of interest

The authors do not have any conflicts of interest to disclose.

Appendix. Comparison of object-agnostic metrics for 2.5D imaging

Due to theoretical considerations, we improved the methodology of Volz *et al* (2024) in several aspects (see table A1). Firstly, we replaced the Gaussian filter by a median filter (Tukey *et al* 1977) due to its ability to preserve edges. Secondly, instead of a Laplacian we use Sobel operators (Danielsson 1990) to determine the gradients in our images. The use of the first derivative entails a smaller sensitivity of the method to noise compared to the Laplacian used in Volz *et al* (2024) which is based on the second derivative as also discussed by the authors themselves.

To experimentally assess the performance of both methods, we applied the sets of kernels listed in table A1 to our data set acquired with the geometric phantom. The size of the kernels was optimized for both methods individually in terms of precision and accuracy. The comparison of the two methodologies is shown in figure A1(a), where the smoothed Laplacian and Tenengrad score, respectively, are plotted as dots over depth. The line represents the smoothed curve, the envelope its uncertainty. The depth, where the maximum score is achieved is marked by an asterisk and diamond, respectively. In (b), the accuracy of the depth determination is shown, where the error bars denote the precision. In figure A1(b) and table A2, it can be seen that our methodology improved the mean precision by around 44%.

Table A1. List of kernels utilized for 2.5D imaging compared to Volz *et al* (2024). The kernel size was individually optimized for each method.

	Volz *et al* (2024)	Presented in this manuscript
Noise reduction	Gaussian (3 px × 3 px)	median (7 px × 7 px)
Gradient determination	Laplacian (7 px × 7 px)	Sobel (3 px × 3 px)

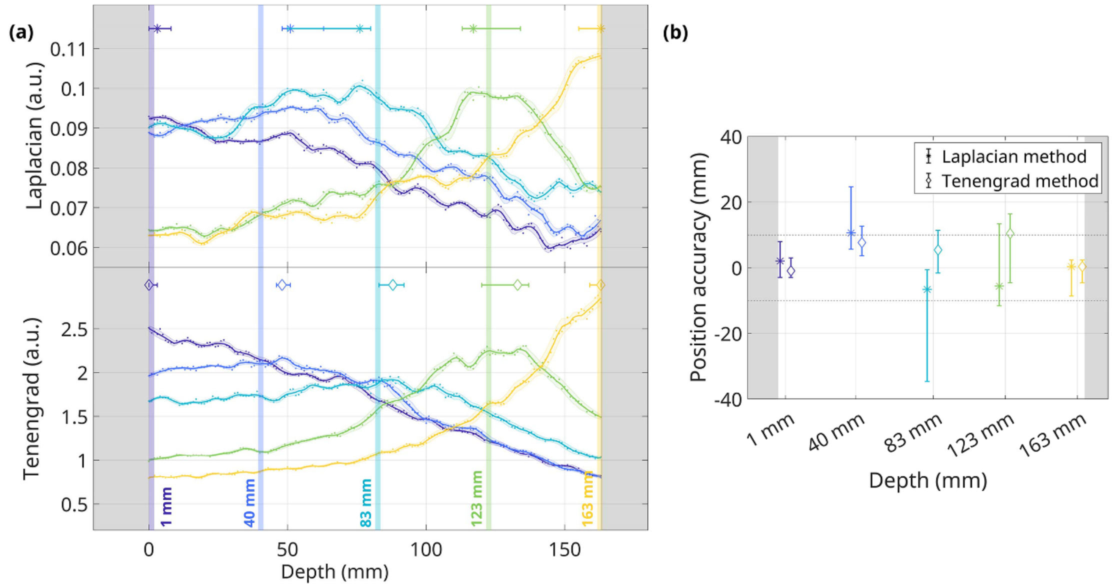

Figure A1. Impact of utilizing different kernels for the 2.5D imaging methodology. We applied the different kernels (see table A1) to our data set acquired with the geometric phantom. In (a), the Laplacian and Tenengrad are shown over depth for all five gap positions. In (b), the accuracy of the depth determination is compared.

Table A2. Accuracy and precision of 2.5D imaging based on different kernels for our data set acquired with the geometric phantom.

	Kernels of Volz *et al* (2024)	Kernels presented in this manuscript
Mean absolute error	5.1 mm	5.0 mm
Mean precision	20.0 mm	11.2 mm

ORCID iDs

Margareta Metzner 0000-0002-6334-1270
Daria Zhevachevska 0009-0003-8910-9968
Patrice Schlegel 0009-0003-6137-0152
Oliver Jäkel 0000-0002-6056-9747
Tim Gehrke 0000-0002-6005-8576

References

Amato C, Martisikova M and Gehrke T 2020 A technique for spatial resolution improvement in helium-beam radiography *Med. Phys.* **47** 2212–21

Barker Jr J L *et al* 2004 Quantification of volumetric and geometric changes occurring during fractionated radiotherapy for head-and-neck cancer using an integrated CT/linear accelerator system *Int. J. Radiat. Oncol. Biol. Phys.* **59** 960–70

Bopp C, Rescigno R, Rousseau M and Brasse D 2014 The impact of tracking system properties on the most likely path estimation in proton CT *Phys. Med. Biol.* **59** N197

Bragg W H and Kleeman R 1905 Xxxix. on the α particles of radium and their loss of range in passing through various atoms and molecules *London Edinburgh Dublin Phil. Mag. J. Sci.* **10** 318–40

Collins-Fekete C-A, Brousmiche S, Portillo S K, Beaulieu L and Seco J 2016 A maximum likelihood method for high resolution proton radiography/proton CT *Phys. Med. Biol.* **61** 8232

Collins-Fekete C-A, Dikaios N, Bär E and Evans P M 2021 Statistical limitations in ion imaging *Phys. Med. Biol.* **66** 105009

Collins-Fekete C-A, Doolan P, Dias M F, Beaulieu L and Seco J 2015 Developing a phenomenological model of the proton trajectory within a heterogeneous medium required for proton imaging *Phys. Med. Biol.* **60** 5071

Collins-Fekete C-A, Volz L, Portillo S K, Beaulieu L and Seco J 2017 A theoretical framework to predict the most likely ion path in particle imaging *Phys. Med. Biol.* **62** 1777

Danielsson P-E and Seger O 1990 Generalized and separable sobel operators *Machine Vision for Three-Dimensional Scenes* (Academic) p 347–79

De Water T A V, Lomax A J, Bijl H P, De Jong M E, Schilstra C, Hug E B and Langendijk J A 2011 Potential benefits of scanned intensity-modulated proton therapy versus advanced photon therapy with regard to sparing of the salivary glands in oropharyngeal cancer *Int. J. Radiat. Oncol. Biol. Phys.* **79** 1216–24

Durante M and Debus J 2018 Heavy charged particles: does improved precision and higher biological effectiveness translate to better outcome in patients? *Seminars in Radiation Oncology* (Elsevier) pp 160–7

Floca R 2009 Matchpoint: on bridging the innovation gap between algorithmic research and clinical use in image registration *World Congress on Medical Physics and Biomedical Engineering*, (*September 7-12, 2009, Munich, Germany: Vol. 25/4*) (*Image Processing, Biosignal Processing, Modelling and Simulation, Biomechanics*) (Springer) pp 1105–8

Fujita H, Tsai D-Y, Itoh T, Doi K, Morishita J, Ueda K and Ohtsuka A 1992 A simple method for determining the modulation transfer function in digital radiography *IEEE Trans. Med. Imaging* **11** 34–39

Gehrke T, Amato C, Berke S and Martišíková M 2018a Theoretical and experimental comparison of proton and helium-beam radiography using silicon pixel detectors *Phys. Med. Biol.* **63** 035037

Gehrke T, Gallas R, Jäkel O and Martišíková M 2018b Proof of principle of helium-beam radiography using silicon pixel detectors for energy deposition measurement, identification and tracking of single ions *Med. Phys.* **45** 817–29

Gianoli C, Bortfeldt J and Schulte R 2024 Ion imaging in particle therapy *Imaging in Particle Therapy: Current Practice and Future Trends* (IOP Publishing) pp 6–1

Gianoli C, Göppel M, Meyer S, Palaniappan P, Rädler M, Kamp F, Belka C, Riboldi M and Parodi K 2020 Patient-specific CT calibration based on ion radiography for different detector configurations in ^{1}H, ^{4}He and ^{12}C ion pencil beam scanning *Phys. Med. Biol.* **65** 245014

Hammi A, Placidi L, Weber D C and Lomax A J 2017 Positioning of head and neck patients for proton therapy using proton range probes: a proof of concept study *Phys. Med. Biol.* **63** 015025

Jakubek J 2011 Precise energy calibration of pixel detector working in time-over-threshold mode *Nucl. Instrum. Methods Phys. Res. A* **633** S262–6

Johnson R P 2017 Review of medical radiography and tomography with proton beams *Rep. Prog. Phys.* **81** 016701

Khellaf F, Krah N, Létang J M and Rit S 2022 Projection deconvolution for proton CT using the spatially variant path uncertainty *IEEE Trans. Radiat. Plasma Med. Sci.* **6** 847–58

Knobloch C *et al* 2022 Experimental helium-beam radiography with a high-energy beam: water-equivalent thickness calibration and first image-quality results *Med. Phys.* **49** 5347–62

Knopf A-C and Lomax A 2013 *In vivo* proton range verification: a review *Phys. Med. Biol.* **58** R131

Kopp B, Meyer S, Gianoli C, Magallanes L, Voss B, Brons S and Parodi K 2020 Experimental comparison of clinically used ion beams for imaging applications using a range telescope *Phys. Med. Biol.* **65** 155004

Krah N, Létang J-M and Rit S 2019 Polynomial modelling of proton trajectories in homogeneous media for fast most likely path estimation and trajectory simulation *Phys. Med. Biol.* **64** 195014

Levin W, Kooy H, Loeffler J S and Delaney T F 2005 Proton beam therapy *Br. J. Cancer* **93** 849–54

Liang X, Mohammadi H, Moreno K C, Beltran C J and Holtzman A L 2025 Heavy ion particle therapy in modern day radiation oncology *Hematol. Oncol. Clin.* **39** 377–97

Llopart X, Ballabriga R, Campbell M, Tlustos L and Wong W 2007 Timepix, a 65k programmable pixel readout chip for arrival time, energy and/or photon counting measurements *Nucl. Instrum. Methods Phys. Res.* **581** 485–94

Lomax A J 2020 Myths and realities of range uncertainty *Br. J. Radiol.* **93** 20190582

Mattes D, Haynor D R, Vesselle H, Lewellyn T K and Eubank W 2001 Nonrigid multimodality image registration *Proc. SPIE* **4322** 1609–20

Metzner M *et al* 2025 Accuracy of a helium-beam radiography system based on thin pixel detectors for an anthropomorphic head phantom *Med. Phys.* **52** 4757–68

Metzner M, Zhevachevska D, Schlechter A, Kehrein F, Schlecker J, Murillo C, Brons S, Jäkel O, Martišíková M and Gehrke T 2024 Energy painting: helium-beam radiography with thin detectors and multiple beam energies *Phys. Med. Biol.* **69** 055002

Miller C *et al* 2019 Reconstructed and real proton radiographs for image-guidance in proton beam therapy *J. Radiat. Oncol.* **8** 97–101

Newhauser W D and Zhang R 2015 The physics of proton therapy *Phys. Med. Biol.* **60** R155–209

Paganetti H, Athar B S, Moteabbed M, Adams J A, Schneider U and Yock T I 2012 Assessment of radiation-induced second cancer risks in proton therapy and IMRT for organs inside the primary radiation field *Phys. Med. Biol.* **57** 6047

Palaniappan P, Meyer S, Kamp F, Belka C, Riboldi M, Parodi K and Gianoli C 2021 Deformable image registration of the treatment planning CT with proton radiographies in perspective of adaptive proton therapy *Phys. Med. Biol.* **66** 045008

Palaniappan P, Meyer S, Rädler M, Kamp F, Belka C, Riboldi M, Parodi K and Gianoli C 2022 X-ray CT adaptation based on a 2D–3D deformable image registration framework using simulated in-room proton radiographies *Phys. Med. Biol.* **67** 045003

Palm Å and Johansson K-A 2007 A review of the impact of photon and proton external beam radiotherapy treatment modalities on the dose distribution in field and out-of-field; implications for the long-term morbidity of cancer survivors *Acta Oncol.* **46** 462–73

Parodi K 2014 Heavy ion radiography and tomography *Phys. Med.* **30** 539–43

Parodi K and Polf J C 2018 *In vivo* range verification in particle therapy *Med. Phys.* **45** e1036–50

Poludniowski G, Allinson N M and Evans P M 2015 Proton radiography and tomography with application to proton therapy *Br. J. Radiol.* **88** 20150134

Reichenbach S E, Park S K and Narayanswamy R 1991 Characterizing digital image acquisition devices *Opt. Eng., Bellingham* **30** 170–7

Rinaldi I, Brons S, Jäkel O, Voss B and Parodi K 2014 Experimental investigations on carbon ion scanning radiography using a range telescope *Phys. Med. Biol.* **59** 3041

Rit S, Dedes G, Freud N, Sarrut D and Létang J M 2013 Filtered backprojection proton CT reconstruction along most likely paths *Med. Phys.* **40** 031103

Romero J *et al* 1995 Patient positioning for protontherapy using a proton range telescope *Nucl. Instrum. Methods Phys. Res. A* **356** 558–65

Sarosiek C *et al* 2021 Analysis of characteristics of images acquired with a prototype clinical proton radiography system *Med. Phys.* **48** 2271–8

Savitzky A and Golay M J 1964 Smoothing and differentiation of data by simplified least squares procedures *Anal. Chem.* **36** 1627–39

Schardt D, Elsässer T and Schulz-Ertner D 2010 Heavy-ion tumor therapy: physical and radiobiological benefits *Rev. Mod. Phys.* **82** 383

Schlag J F, Sanderson A C, Neuman C P and Wimberly F C 1983 *Implementation of Automatic Focusing Algorithms for a Computer Vision System With Camera Control* (Carnegie-Mellon University, The Robotics Institute)

Schneider U and Pedroni E 1994 Multiple coulomb scattering and spatial resolution in proton radiography *Med. Phys.* **21** 1657–63

Schneider U and Pedroni E 1995 Proton radiography as a tool for quality control in proton therapy *Med. Phys.* **22** 353–63

Schulte R W, Bashkirov V, Klock M C L, Li T, Wroe A J, Evseev I, Williams D C and Satogata T 2005 Density resolution of proton computed tomography *Med. Phys.* **32** 1035–46

Schulz-Ertner D and Tsujii H 2007 Particle radiation therapy using proton and heavier ion beams *J. Clin. Oncol.* **25** 953–64

Schweins L, Kirchgässner R, Ochoa-Parra P, Winter M, Harrabi S, Mairani A, Jäkel O, Debus J, Martišíková M and Kelleter L 2025 Detection of an internal density change in an anthropomorphic head phantom via tracking of charged nuclear fragments in carbon-ion radiotherapy *Med. Phys.* **52** 2399–411

Simard M, Fullarton R, Volz L, Schuy C, Robertson D G, Toltz A, Baker C, Beddar S, Graeff C and Fekete C-A C 2025 A comparison of carbon ions versus protons for integrated mode ion imaging *Med. Phys.* **52** 3097–106

Tenenbaum J M 1971 *Accommodation in Computer Vision* (Stanford University)

Thariat J, Hannoun-Levi J-M, Myint A S, Vuong T and Gérard J-P 2013 Past, present and future of radiotherapy for the benefit of patients *Nat. Rev. Clin. Oncol.* **10** 52–60

Tukey J W *et al* 1977 *Exploratory Data Analysis* vol 2 (Springer)

Volz L, Collins-Fekete C-A, Piersimoni P, Johnson R P, Bashkirov V, Schulte R and Seco J 2017 Stopping power accuracy and achievable spatial resolution of helium ion imaging using a prototype particle ct detector system *Curr. Directions Biomed. Eng.* **3** 401–4

Volz L, Collins-Fekete C-A, Sølie J R and Seco J 2020 Theoretical considerations on the spatial resolution limit of single-event particle radiography *Biomed. Phys. Eng. Express* **6** 055002

Volz L, Graeff C, Durante M and Collins-Fekete C-A 2024 Focus stacking single-event particle radiography for high spatial resolution images and 3d feature localization *Phys. Med. Biol.* **69** 024001

Wilson R R 1946 Radiological use of fast protons *Radiology* **47** 487–91